

## Pseudo rigid body model for a nonlinear folding compliant mechanism

Hargrove, Brianne; Nastevska, Angela; Frecker, Mary; Jovanova, Jovana

**DOI**

[10.1016/j.mechmachtheory.2022.105017](https://doi.org/10.1016/j.mechmachtheory.2022.105017)

**Publication date**

2022

**Document Version**

Final published version

**Published in**

Mechanism and Machine Theory

**Citation (APA)**

Hargrove, B., Nastevska, A., Frecker, M., & Jovanova, J. (2022). Pseudo rigid body model for a nonlinear folding compliant mechanism. *Mechanism and Machine Theory*, 176, Article 105017. <https://doi.org/10.1016/j.mechmachtheory.2022.105017>

**Important note**

To cite this publication, please use the final published version (if applicable). Please check the document version above.

**Copyright**

Other than for strictly personal use, it is not permitted to download, forward or distribute the text or part of it, without the consent of the author(s) and/or copyright holder(s), unless the work is under an open content license such as Creative Commons.

**Takedown policy**

Please contact us and provide details if you believe this document breaches copyrights. We will remove access to the work immediately and investigate your claim.

***Green Open Access added to TU Delft Institutional Repository***

***'You share, we take care!' - Taverne project***

**<https://www.openaccess.nl/en/you-share-we-take-care>**

Otherwise as indicated in the copyright section: the publisher is the copyright holder of this work and the author uses the Dutch legislation to make this work public.



ELSEVIER

Contents lists available at ScienceDirect

# Mechanism and Machine Theory

journal homepage: [www.elsevier.com/locate/mechmt](http://www.elsevier.com/locate/mechmt)

Research paper

## Pseudo rigid body model for a nonlinear folding compliant mechanism

 Brianne Hargrove<sup>a,\*</sup>, Angela Nastevska<sup>b</sup>, Mary Frecker<sup>a</sup>, Jovana Jovanova<sup>c</sup>
<sup>a</sup> Penn State University, University Park, PA 16802, United States

<sup>b</sup> Kentaur-Impex, Str. 516 no. 1, Skopje, Republic of North Macedonia

<sup>c</sup> Delft University of Technology, Mekelweg 5, 2628 CD Delft, the Netherlands

### ARTICLE INFO

#### Keywords:

Compliant mechanisms  
Pseudo rigid body model  
Superelasticity  
Hyperelasticity  
Shape memory alloys  
3D-printing

### ABSTRACT

Folding compliant mechanisms have the potential to be used for innovative designs tailored for specific applications such as energy absorption, shape morphing, or stress relief. This tailorability relies on multiple variables that define the geometric and material behavior. The combined effort of the geometric and material nonlinearity can emphasize certain features in the design that, individually, would not be possible. Folding as a concept is very important in origami engineering and requires careful choice in the design variables when it comes to dimensions and material properties. Finite element analyses for folding at the level of a unit cell, as well as the overall structural design, can be cumbersome and computationally expensive. Therefore, in this work, a segmented pseudo rigid body model that captures a high level of flexibility is developed for both a superelastic material, which is characterized using a shape memory alloy, and a hyperelastic, rubber-like material. By increasing the number of segments, the model allows the structure to undergo large deformations. The results from the segmented model are compared with FEA for the folding compliant mechanism. 3D-printing and experimental testing of the compliant mechanism is also explored.

### 1. Introduction

Compliant Mechanisms (CMs) use the elastic deformation of flexible members to transform force, motion, and energy. Contact-aided compliant mechanisms are a special class of CMs that incorporate contact surface(s) for non-smooth path generation or tailoring nonlinear structural stiffness [1–5]. Our research group has developed metamaterial-like arrays of contact-aided compliant mechanisms called cellular contact-aided compliant mechanisms (C3Ms). C3Ms have been shown to provide improvements over their non-contact counterparts for applications like stress relief [6–8] and energy absorption [9,10]. We have also demonstrated the benefits of using superelastic and functionally graded materials in C3Ms in terms of energy absorption [10,11]. By optimizing the geometry of C3Ms with angled compliant joints (ACJs), tailoring of bidirectional nonlinear stiffness has been demonstrated, allowing for both in-plane and out-of-plane bending in bend and sweep CMs [12]. Other researchers have also examined the potential of C3Ms through adding contact in cross-axis flexural pivots to tune rotational stiffness [13]. There is great interest in the use of C3Ms in bio-mimetic design to model the behavior of joints, such as those in the human finger [14,15].

In the literature, various methods have been proposed to model and design CMs under large deformations. Recent developments in

\* Corresponding author.

E-mail address: [bbh5128@psu.edu](mailto:bbh5128@psu.edu) (B. Hargrove).

<https://doi.org/10.1016/j.mechmachtheory.2022.105017>

Received 21 February 2022; Received in revised form 1 June 2022; Accepted 1 July 2022

Available online 11 July 2022

0094-114X/© 2022 Elsevier Ltd. All rights reserved.

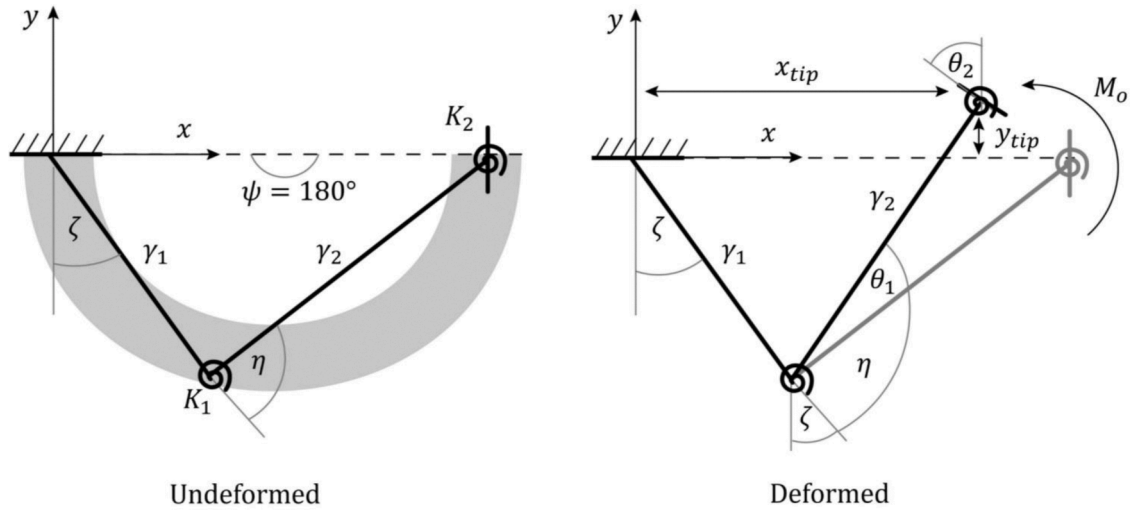


Fig. 1. PRBM for a semicircular arc loaded with a moment on the tip using two links and two torsional springs.

topology optimization have used hyperelastic or non-Hookean materials to model the geometric nonlinearity of CMs through finite element analysis (FEA) [16–18]. Prior to these developments, topology optimization for synthesis of compliant mechanisms has involved the use of nonlinear beam elements to account for large deformations in preexisting, linear finite element methods [19]. The topology optimization approach has been applied to micro-CMs with geometrically nonlinear structural behavior [20]. Nonlinear stress and strain measures replace linear Cauchy stress assumptions for these CMs, but they still remain under the assumption of a linear elastic material model [21]. Cellular structures comprised of CM unit cells have been optimized for a desired compliance with the assumption of a linear displacement profile [22]. There are also FEA models that simulate the nonlinear deflection of compliant beam elements, considering Hookean material behavior [23]. In general, these FEA-based CM design methods consider large deformation behavior through geometric nonlinearity, but are limited to linear material behavior.

Pseudo rigid body models (PRBMs) approximate a compliant mechanism with rigid links and torsional springs and are widely used to account for large deformations in compliant mechanisms, cf. [24]. However, a limitation of PRBMs is that they have been developed only for linear materials. PRBMs have been used to model contact-aided compliant mechanisms with nonlinear deflection via contact-aided linear-elastic beams [25]. Compliant parallel mechanisms used in bicycle brakes have been designed using the large deflection theory of the PRBM [24], but using Hookean relationships for anisotropic materials, such as fiberglass [26]. PRBMs have been developed to model large deflection of flexural beams with an inflection point for linear elastic materials [27]. Using beam theory, analytical and FEA models have demonstrated the selective compliance of curved flexure hinges [28]. However, this approach considered linear elastic behavior and small deformations. Design of compliant mechanisms incorporating both geometric and material nonlinearity, using FEA-based models or PRBMs, has yet to be explored.

In this paper, we propose a method to account for geometric and material nonlinearity in the PRBM for two case studies: superelastic NiTi and hyperelastic thermoplastic polyurethane (TPU). To the authors' knowledge, there has not been prior work accounting for both sources of nonlinearity in the PRBM, specifically for CMs. The CM used for the PRBM was introduced by our group and investigated for large scale shape change applications [29]. In our previous work, the design is called a “folding C3M” due to its similarity to a compliant hinge and its ability to experience large folding-like deformations and stress relief through self-contact. While the design consists of a contact surface to simulate stress-relief in a C3M, self-contact is not investigated in this paper and is addressed in the future work section. As a result, the design will be referred to as a “folding CM” since only the unconstrained, flexible direction of the CM without self-contact is modeled. The following section discusses the development of the PRBM for this nonlinear, folding CM.

## 2. Methods

### 2.1. Pseudo rigid body model (PRBM)

The PRBM is an analytical method for simplifying the analysis of CMs by using rigid links and springs to model flexible segments, which are then used to predict the relationship between the applied loads and the deflection. The folding CM is represented by a semicircular arc connected to frames on each end, where loads and constraints can be applied [29]. The arc is assumed to be the most flexible region of the CM, while the rest of the mechanism is assumed to be rigid. In this section, a segmented PRBM of solely the arc is developed for large deflections, and then extended to include nonlinear material behavior in the next section.

In the literature, a PRBM for a semicircular arc CM with linear material behavior was developed [30]. This model is used as a starting point for analyzing the deformation of the folding CM and is summarized briefly here. The PRBM shown in Fig. 1 consists of two rigid links with lengths (\(\gamma\_1\) and \(\gamma\_2\)), and two torsional springs with stiffnesses (\(K\_1\) and \(K\_2\)). The angle (\(\psi\)) is a constant value of \(180^\circ\)

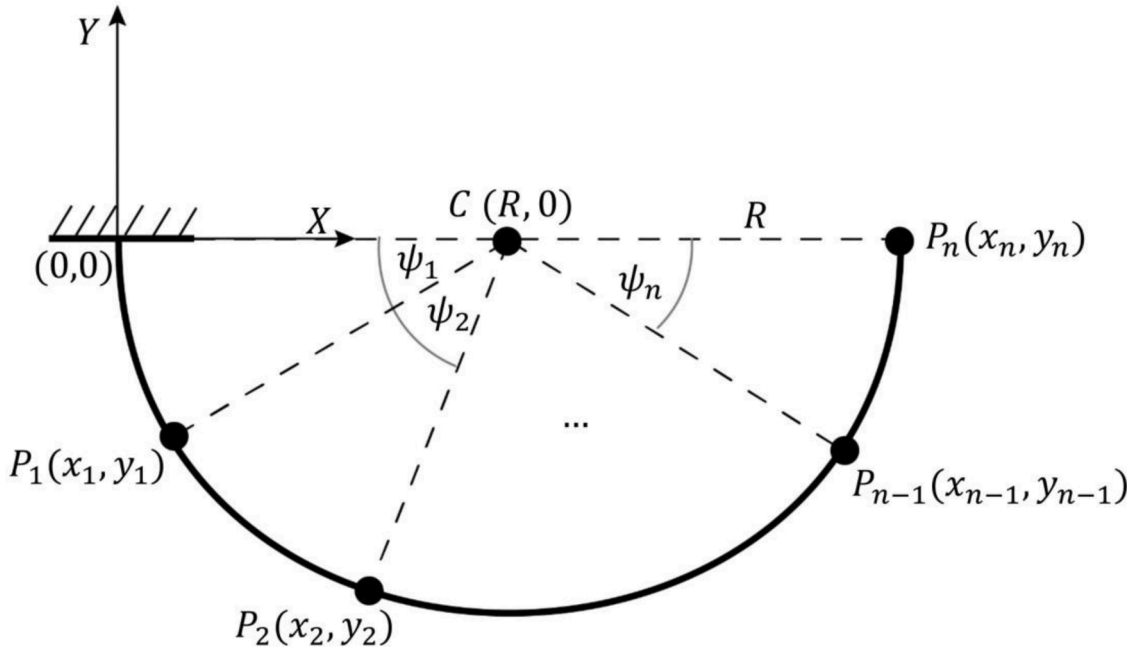


Fig. 2. Global coordinate system of the semicircular arc segmented into n number of segments and the corresponding tip locations for each segment.

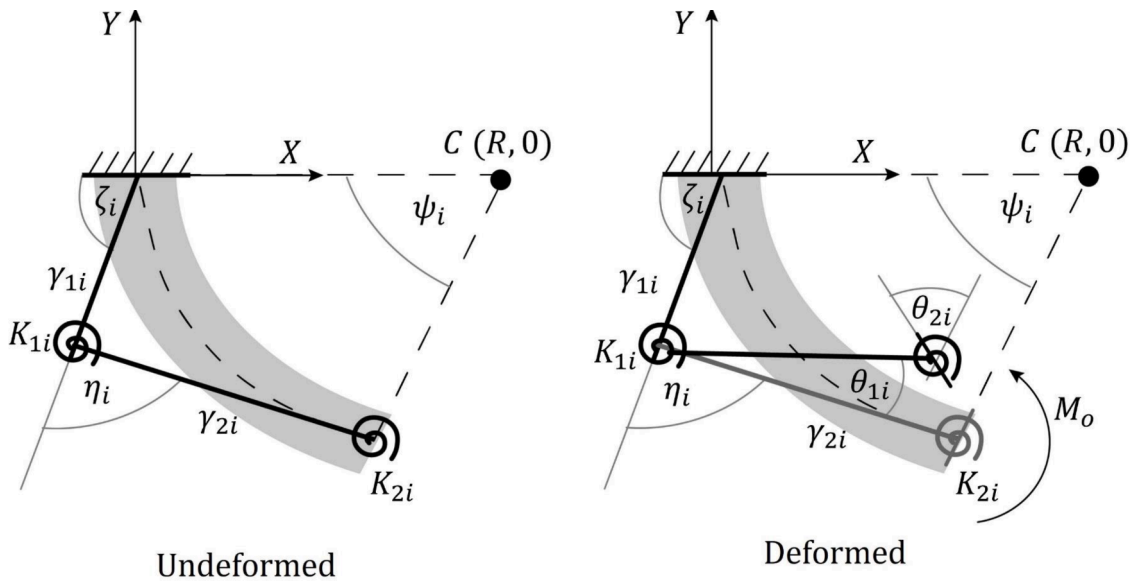


Fig. 3. PRBM representation of each segment of the semicircular arc with sector angle ψi.

for a semicircular arc. As the arc is being deformed due to the applied moment (Mo), the angles of displacement (θ1 and θ2) increase. The PRBM parameters were estimated in [30] for different angles (ψ) with the objective of decreasing the error between the PRBM and the beam theory model.

By using the estimated values of the PRBM parameters (ζ, η, γ1, γ2, K1, K2), for ψ = 180°, the deformation of the tip can be estimated as shown in Fig. 1. The relationship between the link rotations (θ1 and θ2) and the external moment (Mo) is given by Eq. (1):

$$\begin{bmatrix} K_1\theta_1 \\ K_2\theta_2 \end{bmatrix} = \begin{bmatrix} 1 \\ 1 \end{bmatrix} [M_o] \tag{1}$$

From Eq. (1), the angular displacements can be calculated as:

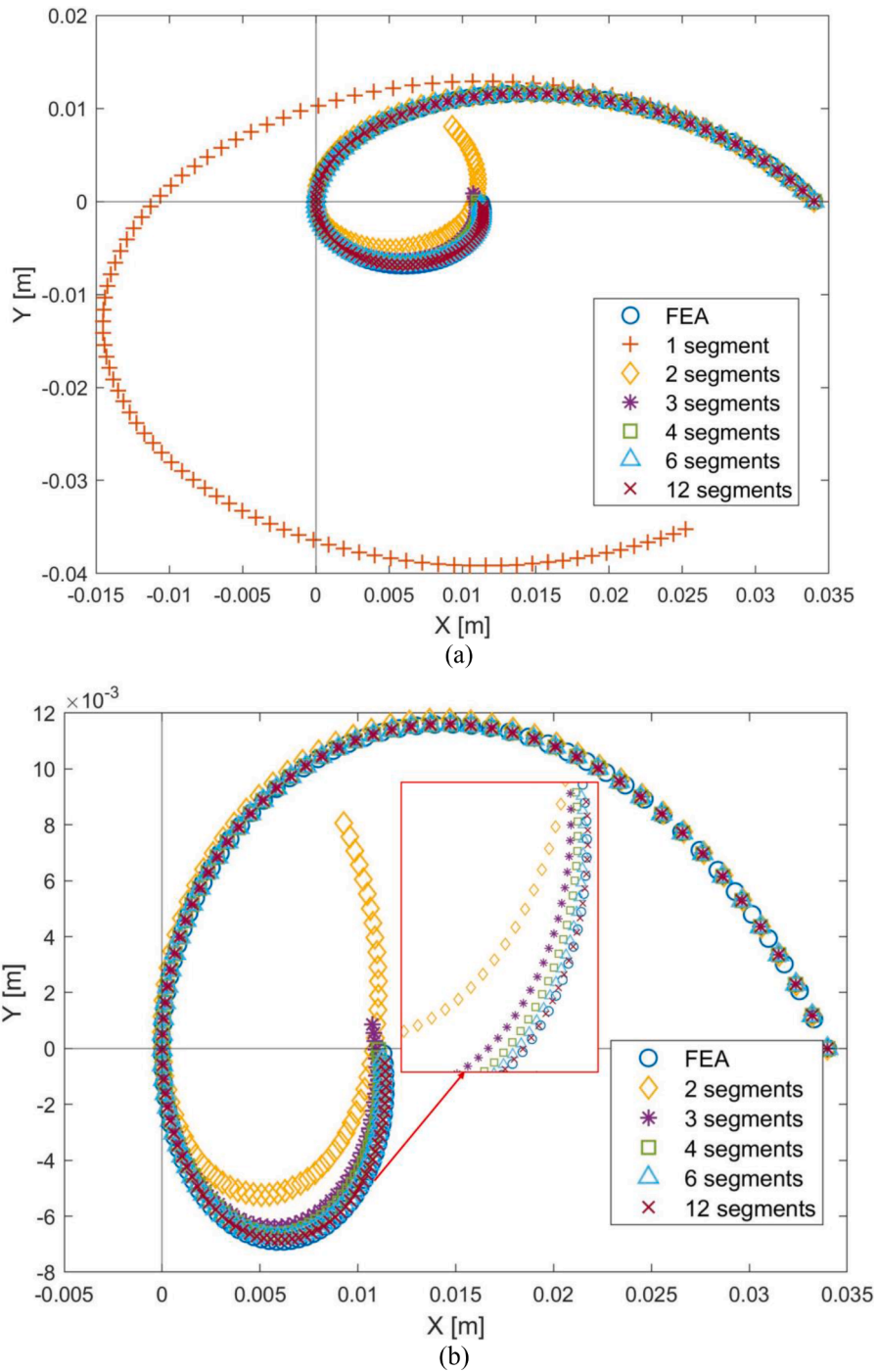


Fig. 4. Comparison of the segmented PRBM tip deflection for  $n = 1$  to 12 segments with FEA (a) and a zoomed in view of the increasing accuracy of the PRBM for a higher number of segments and a rotation of  $2\pi$  rad (b).

**Table 1**  
MSE between FEA and PRBM tip deflection for a linear-elastic material and a different number of segments

Number of segments	MSE (m <sup>2</sup> )
1	5.11e-04
2	1.40e-05
3	3.03e-06
4	2.58e-06
6	2.49e-06
12	2.48e-06

$$\theta_i = \frac{M_o}{K_i} \quad i = 1, 2 \quad (2)$$

The torsional stiffnesses ( $K_i$ ) are a function of the nondimensional stiffness coefficients  $k_{\theta_i}$ , where:

$$K_i = k_{\theta_i} \frac{EI}{L} \quad i = 1, 2 \quad (3)$$

In Eq. (3), the material and geometric parameters are defined as the elastic modulus of the material ( $E$ ), the area moment of inertia of the cross-section ( $I$ ), and the beam length ( $L$ ) or the perimeter of a semicircle with radius ( $R$ ). By combining Eq. (2) and Eq. (3), the angular deformations become:

$$\theta_i = \frac{M_o L}{k_{\theta_i} EI} \quad i = 1, 2 \quad (4)$$

It was found that the accuracy of this model is not sufficient for large deformations since the behavior of the entire semicircular arc is captured using only one PRBM with two torsional springs to tailor the stiffness. Therefore, we have developed a segmented model where the semicircular arc is divided into a number of continuously connected segments. The arc is divided into  $n$  segments, each defined by the angle  $\psi_i$  as shown in Fig. 2. The segments are assumed to be geometrically identical, and the angle of each sector is  $\psi_i = \psi = \pi/n$ . Each segment is represented by a PRBM with two torsional springs and two rigid links as shown in Fig. 3. The angles  $\zeta_i$  and  $\eta_i$  depend on the angle  $\psi_i$  and the number of segments ( $n$ ).

The coordinates of the end of each segment are calculated locally as:

$$x_{local,i} = [\gamma_{1i} \sin \zeta_i + \gamma_{2i} \sin(\zeta_i + \eta_i + \theta_{1i})] \cdot \frac{L}{n} \quad i = 1, 2, \dots, n \quad (6)$$

$$y_{local,i} = [-\gamma_{1i} \cos \zeta_i - \gamma_{2i} \cos(\zeta_i + \eta_i + \theta_{1i})] \cdot \frac{L}{n} \quad i = 1, 2, \dots, n \quad (7)$$

The angles  $\theta_{1i}$  and  $\theta_{2i}$  are the angular deformations of the two torsional springs from Eq. (2). The torsional stiffnesses of the two springs ( $K_{1i}$  and  $K_{2i}$ ) are defined using the nondimensional stiffness coefficients in Eq. (3). Coordinate transformation is used to relate the local and global measures of the position of each segment, the details of which can be found in Appendix A.

The effect of the number of segments ( $n$ ) on the tip displacement was explored with a 2D FEA model in COMSOL Multiphysics. The structural mechanics module was used with the fully coupled approach with an automatic physics-controlled mesh (maximum element size of 3.8E-4 m and minimum element size of 7.6E-7 m). The FEA model has a 4 mm in-plane thickness, 30 mm inner diameter, and assumes a 1 m out-of-plane thickness. Geometric nonlinearity is included, but the material behavior is chosen to be linear with an elastic modulus ( $E$ ) of 70 GPa. The arc is subjected to a prescribed rotation at the free end varying from 0 to  $2\pi$  radians. The corresponding reaction moments serve as inputs to the PRBM in MATLAB for the purposes of comparison, and are applicable only for the material and geometry defined for this specific model.

In Fig. 4, the tip position of the segmented PRBM for a different number of segments is presented, along with the FEA prediction for each chosen value of  $n$ . Physically, the maximum possible rotation of the tip is  $\pi$  radians. However, for the purpose of analysis, the model is deformed until  $2\pi$  radians and self-collision is not considered. It is evident that the PRBM using one segment, marked in orange in Fig. 4(a), overestimates the tip deflection predicted by the FEA model. For a higher number of segments ( $n$ ), the estimation of the tip deflection by the segmented PRBM becomes more accurate. The impact of the number of segments on the accuracy of the model depends on the level of deformation. For smaller amounts of deformation, even the model with one segment agrees well with the FEA results. As the deformation increases beyond  $\pi/2$  radians, the distinction between the PRBMs for a single segment and for multiple segments increases. Although a higher number of segments is more accurate in predicting the position of the tip of the arc overall, there is not much of a difference between the curves until the rotation goes beyond the physical maximum deformation of  $\pi$  radians.

As the deformation approaches  $2\pi$  radians, Fig. 4(b) shows that increasing the number of segments increases the accuracy of the model as well. This means that for the rotation needed for full folding (the maximal physical deformation of  $\pi$  radians), the segmented model with 2 segments is a good enough approximation of the tip deflection. The accuracy of the segmented PRBM is quantified by the mean-squared error (MSE) of the tip deflection up to  $2\pi$  radians, as shown in Table 1. The MSE is one order lower for the model with 2 segments compared to one. Additionally, the error decreases as the number of segments increases.

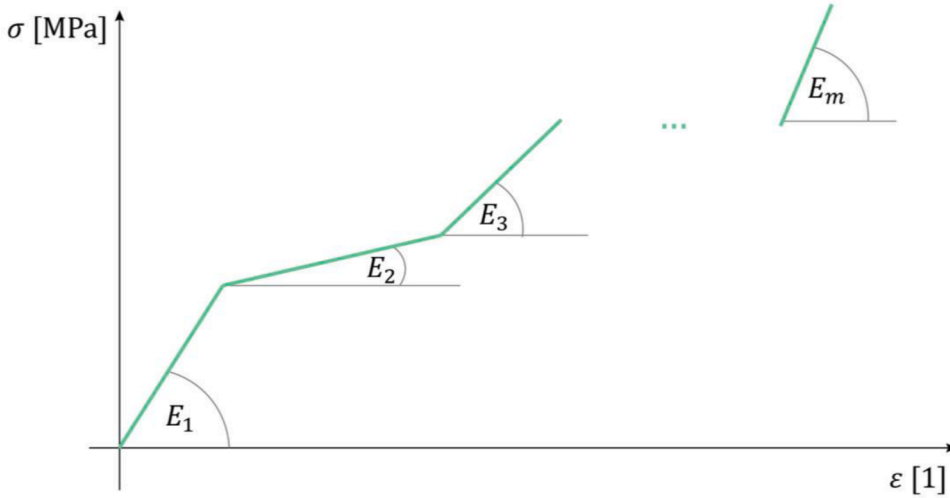


Fig. 5. General multilinear model of a nonlinear material with  $m$  number of sections, with each section having a slope equal to the elastic moduli ( $E_1$  to  $E_m$ ).

### 2.2. Modeling nonlinear stiffness

The segmented PRBM predicts the tip position, or the  $x$  and  $y$  coordinates, of the CM after it is loaded (Eq. (A.6) and Eq. (A.7) in Appendix A). In these equations, the only variables that depend on the load are the angles of deformation of the two torsional springs ( $\theta_{1i}$  and  $\theta_{2i}$ ). To calculate these angles, Eq. (4) is used where the nondimensional stiffness coefficient ( $k_{\theta i}$ ), the area moment of inertia ( $I$ ), and the circumference of the arc ( $L$ ) are related only to the geometry. Therefore, only the elastic modulus ( $E$ ) can be changed to introduce material nonlinearity into the PRBM. To achieve this, we propose a method for the elastic modulus to be defined as a function of the applied moment.

In Fig. 5, a nonlinear material can be approximated using a multilinear model with  $m$  number of linear sections. Each section has a different slope representing the elastic modulus, which changes once a critical stress is reached. The nonlinear material can be symmetric or asymmetric in tension and compression, and can have any number of linear sections ( $m$ ), in each direction.

Since the effective elastic modulus of a nonlinear material is a function of the stresses, the spatial distribution of this property also depends on the spatial distribution of the stresses, and is not uniform as a result. Therefore, an average modulus is used in the PRBM. This effective modulus, denoted by  $E_n$ , is a function of the input load and depends on both the material and the geometry.  $E_n$  can be calculated using Eq. (8) by substituting the bending moment ( $M_0$ ), the angle of rotation ( $\theta$ ), the circumference of the arc ( $L$ ), and the moment of inertia ( $I$ ). This equation can be derived using Castigliano’s Method or from beam deflection theory for pure bending. The bending moment and angle of rotation can be extracted either from experimental measurements or from an FEA model of the mechanism.

$$E_n = \frac{M_0}{\theta} \cdot \frac{L}{I} \tag{8}$$

Similar to the approximation of the material model itself, this function is approximated as a multilinear model of the effective modulus ( $E_{eff}$ ) shown in Eq. (9), where  $M$  is the applied moment. This multilinear approximation provides the opportunity to relate  $E_n$  to the moduli of the material model ( $E_1$  to  $E_m$ ). The multilinear model consists of  $m$  linear equations, where the coefficients  $a_1$  to  $a_m$  and  $b_1$  to  $b_m$  depend on the moduli ( $E_1$  to  $E_m$ ) shown in Fig. 5. The critical moments,  $M_{cr1}$  to  $M_{crm}$  depend on the critical stresses of the material model.

$$E_{eff} = \begin{cases} a_1 \cdot M + b_1; \text{for } M \leq M_{cr1} \\ a_2 \cdot M + b_2; \text{for } M_{cr1} < M < M_{cr2} \\ \dots \\ a_m \cdot M + b_m; \text{for } M \geq M_{crm} \end{cases} \tag{9}$$

By substituting the elastic modulus ( $E$ ) in Eq. (3) of the PRBM with the expressions of the effective modulus ( $E_{eff}$ ) in Eq. (9), the nonlinearity of the material is taken into consideration. In other words, the stiffnesses of the torsional springs ( $K_i$ ) include the modulus as a nonlinear function of the applied moment.

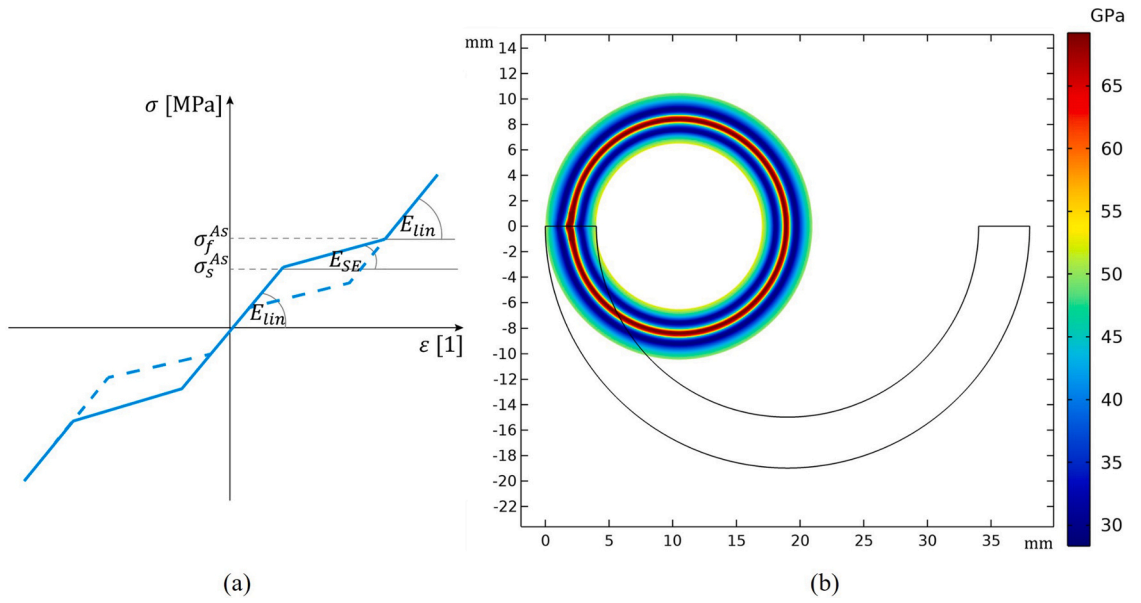


Fig. 6. NiTi material model derived as a multilinear function with tension-compression symmetry (a) and the spatial distribution of the effective modulus in GPa for a rotation of  $\pi$  rad (b).

### 3. Case studies

#### 3.1. Superelastic NiTi

Nickel-titanium (Nitinol or NiTi) is a “smart” material that exhibits shape memory behavior and superelasticity. In this case study, only the stress-induced phase transformation experienced by shape memory alloys (SMAs), known as superelasticity, is considered. It is assumed that there is no temperature-induced phase transformation or shape memory behavior. The superelastic behavior of NiTi is attractive for CM design, allowing for up to 10% recoverable elastic deformation [32].

##### 3.1.1. Material model

The multilinear material model for NiTi developed in [31] is shown in Fig. 6(a), where it is noticeable that once the critical transformational stress  $\sigma_s^{AS}$  is achieved, the slope of the modulus of elasticity  $E_{lin}$  decreases to  $E_{SE}$ . The spatial distribution of the effective modulus of a semicircular arc comprised of superelastic NiTi can be seen in Fig. 6(b) for a rotation of  $\pi$  radians, as predicted by COMSOL Multiphysics.

The effective modulus for NiTi is represented by three linear sections, corresponding to the superelastic material model in Fig. 6(a). The generalized equations in Eq. (9) are reduced to Eq. (10) by using prescribed rotation ( $\theta$ ) and the corresponding reaction moment ( $M_o$ ) from FEA to determine  $E_n$  in Eq. (8). Then, the critical moments are used to define the expressions for the effective modulus ( $E_{eff}$ ) as a multilinear function. In the first section, the effective modulus is  $E_{lin}$  until critical moment,  $M_{cr}$ , is reached. Then, it is followed by a linearly decreasing modulus  $h \cdot E_{lin}$ . This decrease reaches a minimum at  $M_{SE}$ , after which the modulus is  $E_{lin} - E_{SE}$ .

$$E_{eff} = \begin{cases} E_{lin}; & \text{for } M \leq M_{cr} \\ h \cdot E_{lin}; & \text{for } M_{SE} > M > M_{cr} \\ E_{lin} - E_{SE}; & \text{for } M \geq M_{SE} \end{cases} \quad (10)$$

The linear function is defined as:

$$h = \left( 1 - \frac{1}{E_{lin} - E_{SE}} \right) \quad (11)$$

The moments ( $M_{cr}$  and  $M_{SE}$ ) mark the start and end of the phase transition region for NiTi, and are related to the critical stresses  $\sigma_s^{AS}$  and  $\sigma_f^{AS}$  of the NiTi material model respectively. The values for these moments are dependent on both the material model as well as the geometry of the CM. The effective modulus functions for two different superelastic materials are shown in Fig. 7(a), while the material models are shown in Fig. 7(b). Material A uses the properties of NiTi from internal measurements made by our collaborators, while Material B is a variation of Material A. Material B could be achieved by adjusting the composition of Ni and Ti within the NiTi alloy, or through heat treatment of the material. The materials have the same transformation stresses, but different elastic moduli and thus different critical moments. Note that only loading of NiTi is considered. The hysteresis that is present upon unloading is not accounted for in this case study.

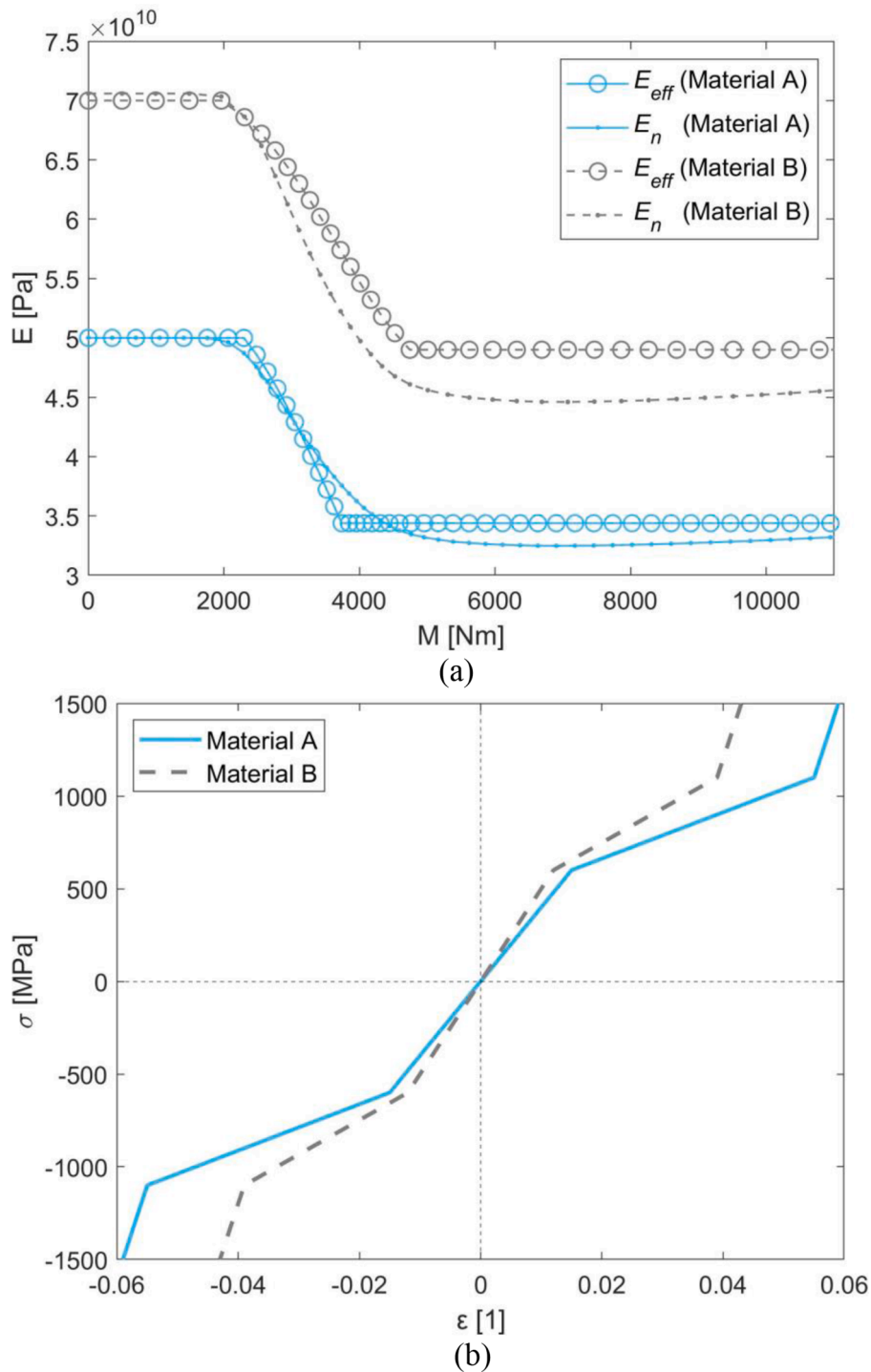
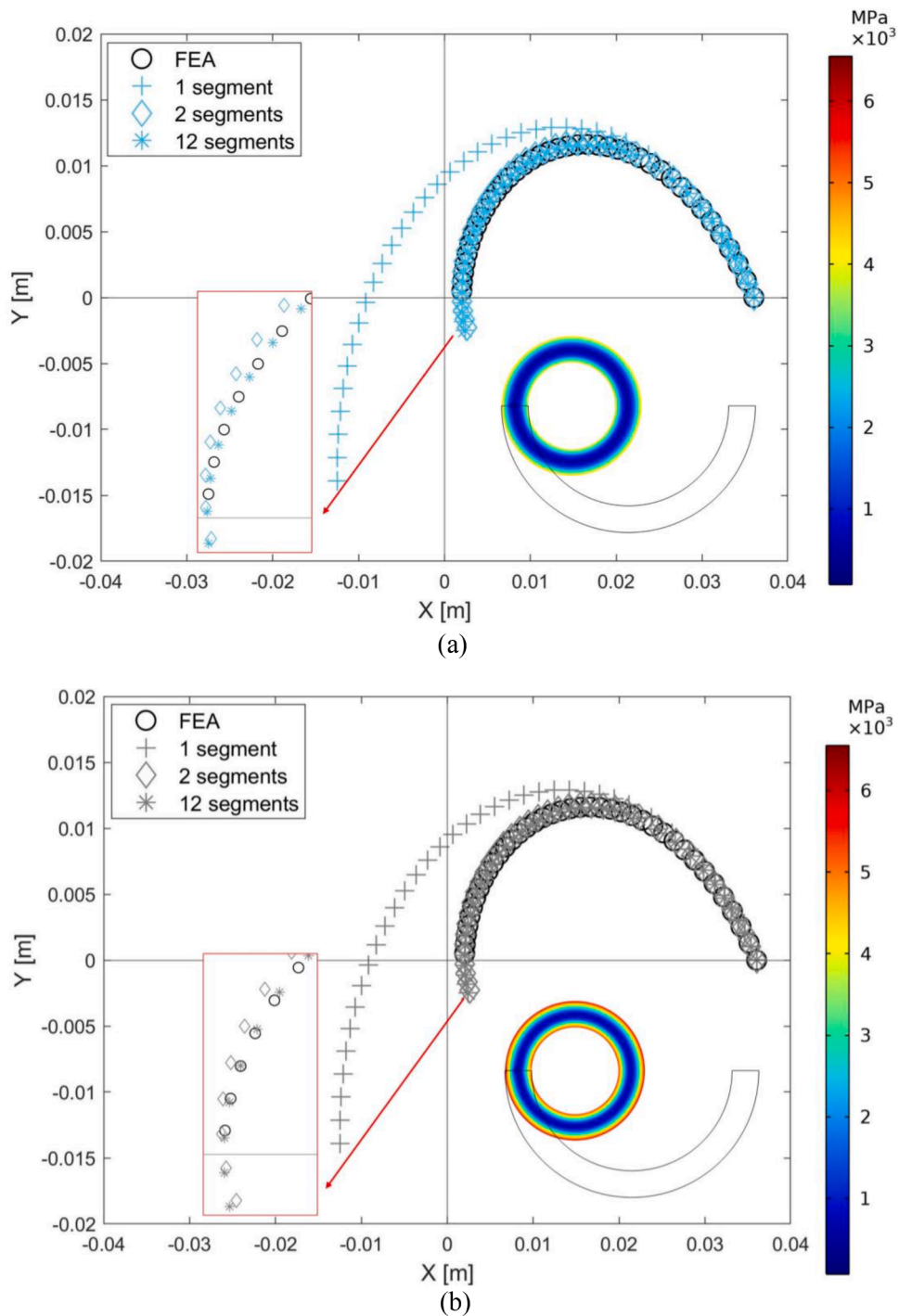


Fig. 7. Plots of the nonlinear effective modulus of elasticity for two different material models, Material A and Material B, of NiTi (a) and the material models of the two variations of NiTi (b).

### 3.1.2. Segmented PRBM

To evaluate the CM in COMSOL using NiTi, a semicircular arc with a 4 mm in-plane thickness, 30 mm inner diameter, and 1 m out-of-plane thickness was used in the FEA model. The material models given in Fig. 7(b) are used as inputs to the FEA models in order to capture the nonlinearity of the two materials A and B. The results of the PRBM are compared to the results of the FEA model, where the maximum deformation is  $\pi$  radians. Fig. 8(a) and (b) show the results of the segmented PRBM for Material A and Material B



**Fig. 8.** Plots of the tip deflection of the segmented PRBM for 1, 2, and 12 segments using material models of Material A (a) and Material B (b) respectively with the corresponding stress distribution in MPa from FEA.

respectively, where the position of the tip of the arc for an increasing moment is presented. The plots show that the single segment PRBM is a poor approximation and the model overpredicts the deflection. The trend is the same as the linear case in that a higher number of segments ( $n$ ) results in a lower MSE between the PRBM and the FEA predictions of the tip deflection.

In this case, however, both the 2 and 12 segment PRBM agree well with FEA compared to the model with one segment. As the color legends in the plots suggest, the arc modeled with Material B experiences higher maximum stresses than the arc with Material A for the same deformation of  $\pi$  radians. For both materials, the transformational stress ( $\sigma_s^{AS}$ ) is the same and equal to 600 MPa. However, as

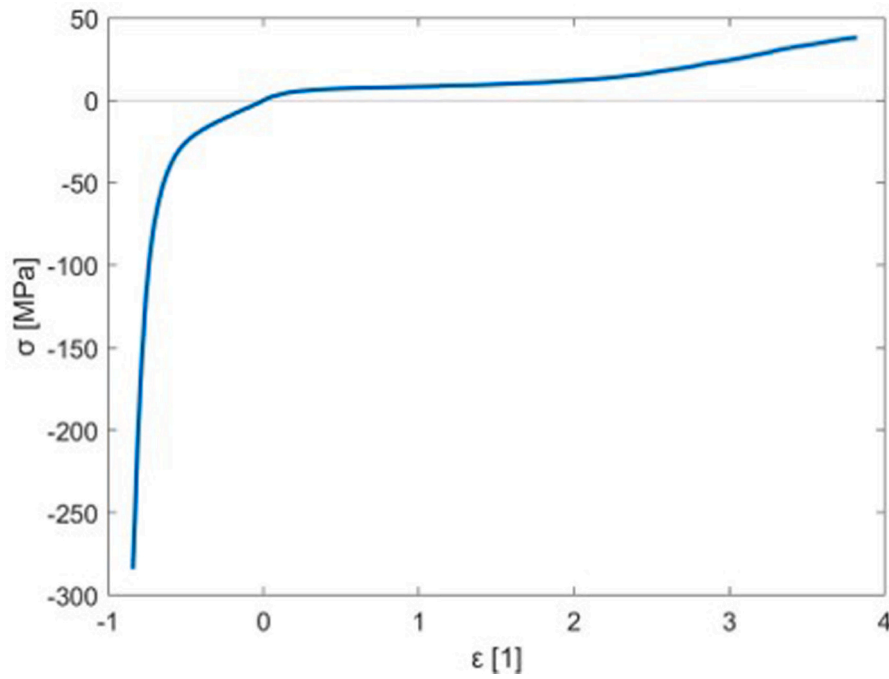


Fig. 9. Nonlinear material model of TPU with tension-compression asymmetry. Adapted from [33].

Table 2

R-squared values based on the number of sections in the multilinear approximation

Number of Sections	R <sup>2</sup>
3	0.23
4	0.89
5	0.99
6	0.99
7	0.99

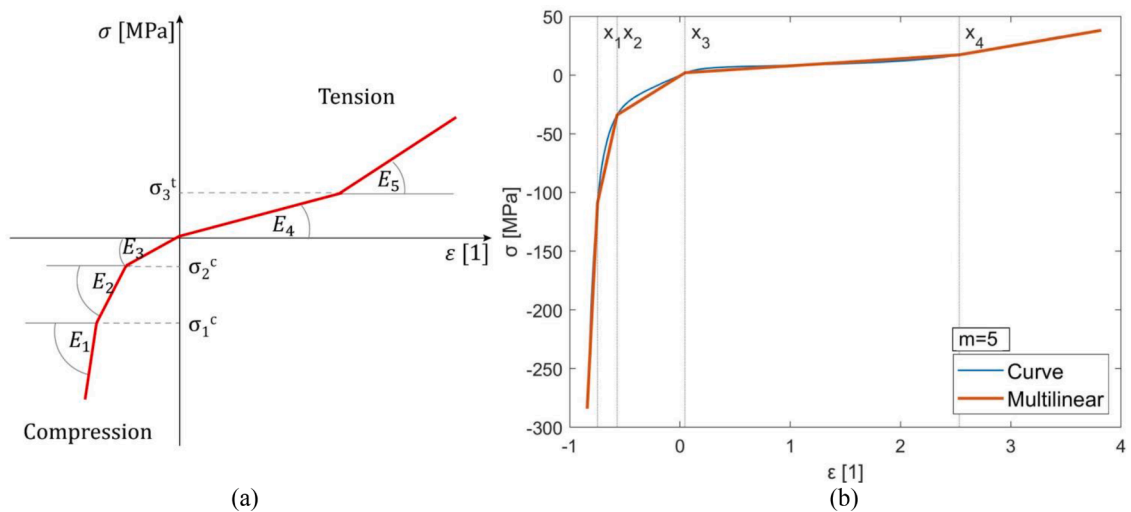
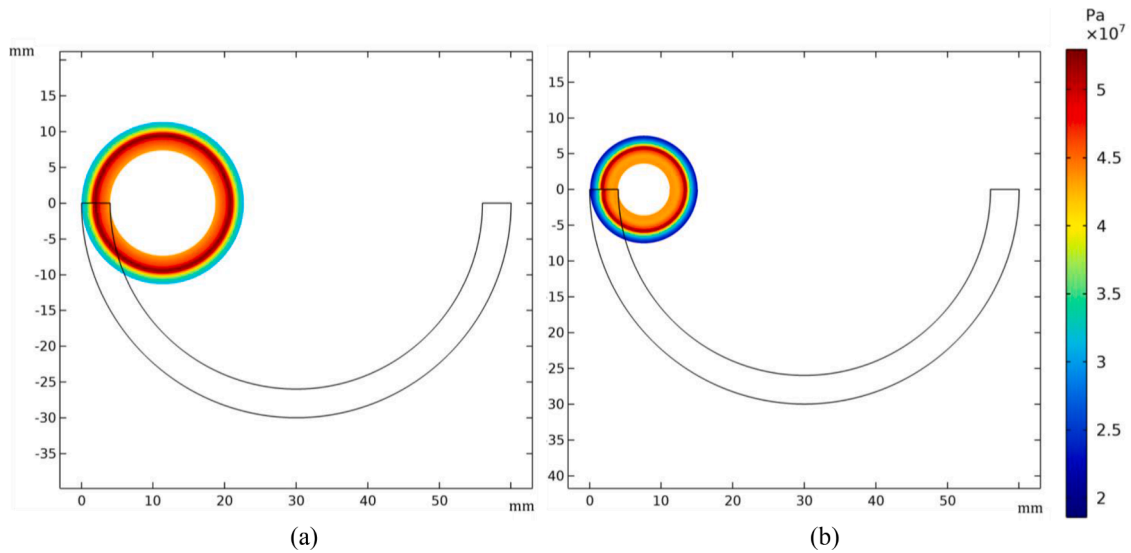


Fig. 10. Multilinear approximation of the behavior of TPU with critical stresses for tension and compression (a) and critical strains for  $m = 5$  sections (b).



**Fig. 11.** Spatial distribution of the effective modulus in MPa measured in COMSOL for deformation of  $2\pi$  rad (a) and  $4\pi$  rad (b) highlighting the tension-compression asymmetry of TPU.

Fig. 7(a) shows, the elastic modulus in the linear part of the curve ( $E_{lin}$ ) is equal to 50 GPa for Material A and 70 GPa for Material B. For this reason, the stress distributions in Fig. 8 indicate that the outer circumference of the arc, which is the location of the highest stresses, transitions into the phase transformation region for different levels of deformation. The transformational stress of 600 MPa is reached for deformation of 0.31 radians for Material A and 0.19 for Material B respectively.

### 3.2. Hyperelastic TPU

A second case study explores the effect of material nonlinearity on the folding CM's behavior, using TPU. TPU is commercially available in filament form for use in fused deposition modeling (FDM) printers or material extrusion (MEX) technology, and can undergo large, nonlinear elastic deformations. The material is assumed to be hyperelastic, which is a property of rubber-like materials. Near incompressibility of a hyperelastic material provides the additional benefit of large shape changes when subject to large strains. For the analytical, FEA, and experimental studies of the folding CM, nonlinearities due to hysteresis, creep, and stress relaxation are not considered.

#### 3.2.1. Material model

Published data by Platek et al [33] was used as the nonlinear material model for TPU. The open-source tool, WebPlotDigitizer [34], was used to extract the data from the uniaxial tensile and compression tests performed on 3D-printed dog-bone specimens. As shown in Fig. 9, the behavior of TPU becomes nonlinear after approximately 10% strain, and the maximum strain that was measured in the uniaxial test is around 380%. This illustrates the highly elastic behavior of TPU. Unlike the multilinear model for NiTi in Fig. 7(a), TPU exhibits asymmetric material behavior in tension and compression.

The material model for TPU is approximated as a multilinear model with  $m$  number of sections, as presented previously for the general approximation in Fig. 6. A threshold on the first derivative of the material model curve was used to determine the critical strains and stresses. The largest percent difference in the derivative, or the largest change in slope, was compared to a target percentage of 50%. Once the percent difference exceeded 50%, this represented the location of a transition point. The R-squared of the multilinear approximation was calculated based on the number of sections, from 3 to 7 sections, as shown in Table 2. The best approximation was one with a R-squared value equal to or greater than 0.99 and that also minimized the number of sections. An approximation with 5 sections, as shown in Fig. 10, satisfies this criterion.

#### 3.2.2. Segmented PRBM

Using the material model for TPU, a semicircular arc with a 4 mm in-plane thickness, 52 mm inner diameter, and 4 mm out-of-plane thickness was modeled in COMSOL for an applied moment at the tip. The spatial distribution of the effective modulus in the arc when deformed up to  $2\pi$  and up to  $4\pi$  is shown in Figs. 11(a) and (b). Although the maximum physical deformation of the arc is  $\pi$  radians, the model was deformed beyond this point for a better depiction of the large deformations. As a result, self-collision is not taken into consideration. Since the material model is asymmetric in tension and compression, the effective modulus is also asymmetric.

The effective modulus,  $E_n$ , versus the applied moment,  $M$ , is shown in Fig. 12, where the dashed lines represent the corresponding angles of rotation for the applied moment. This nonlinear relationship is defined with three sections. All of the three sections that illustrate the nonlinearity of the effective modulus are located within a deformation range up to  $\pi$  radians, marked by the red rectangle.

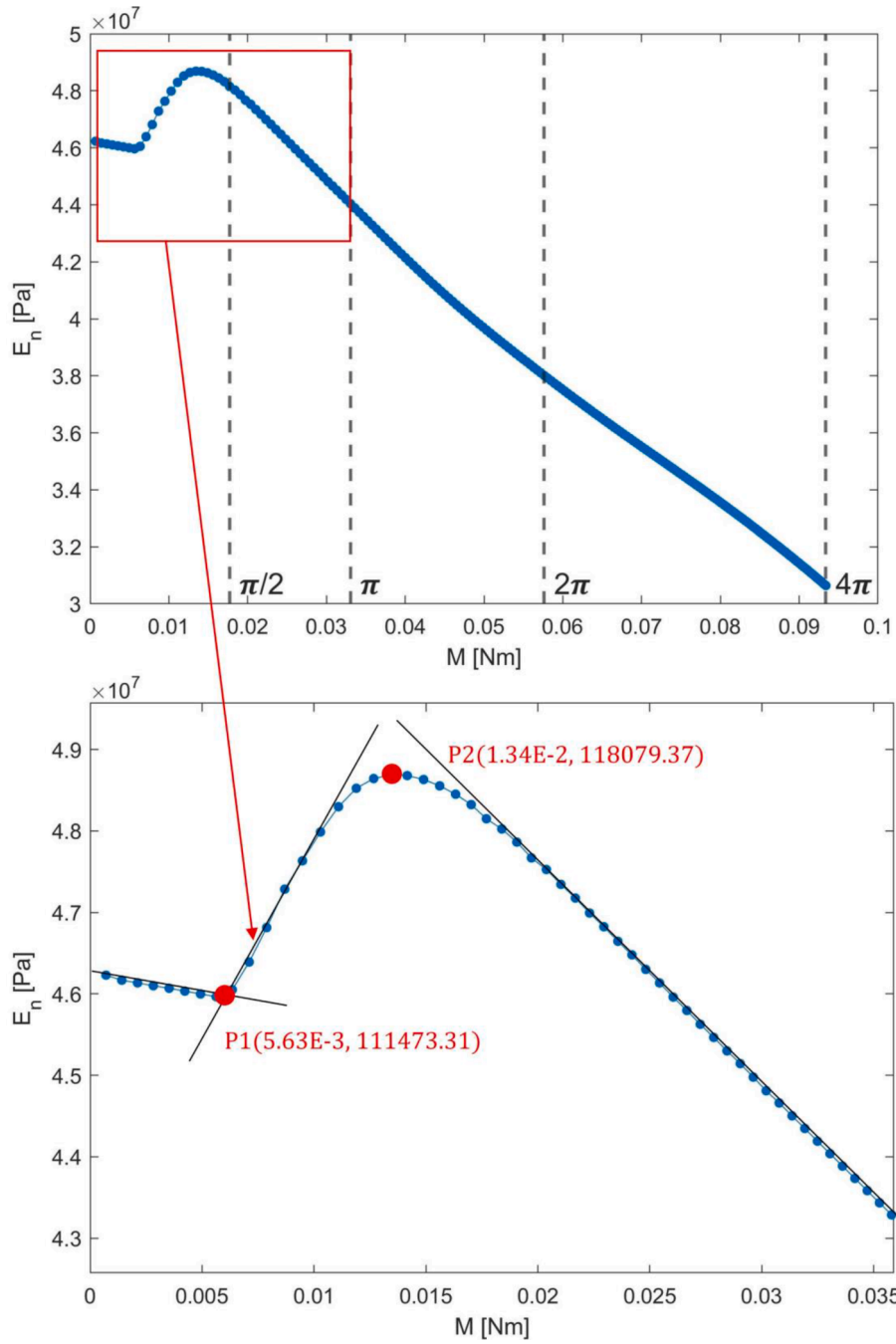
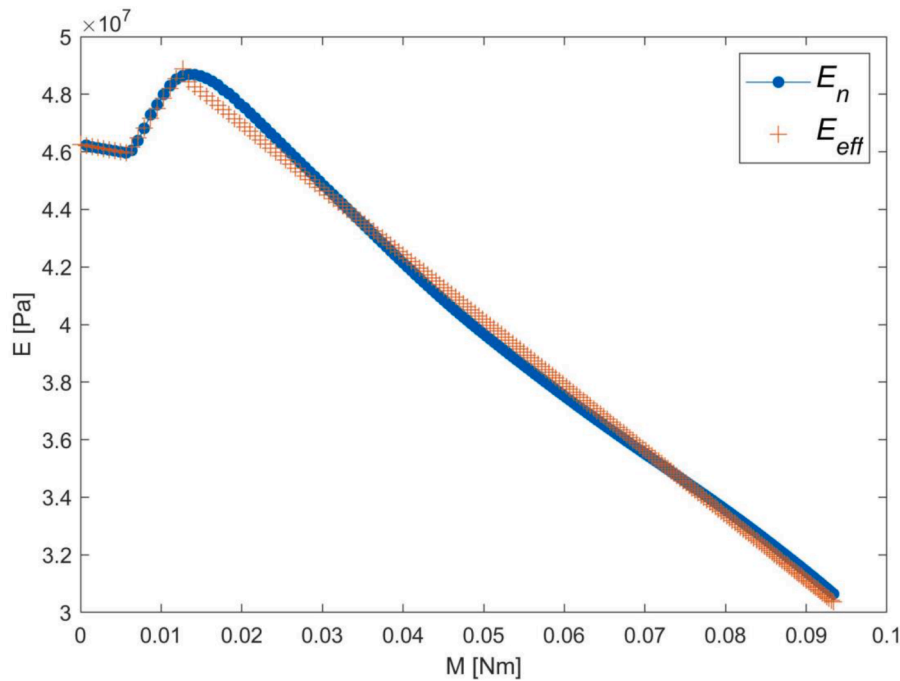


Fig. 12. The effective modulus ( $E_n$ ) vs the moment ( $M$ ) depicting the nonlinearity of the effective modulus and the location of the critical moments marked by red dots.

The local minimum and maximum points (P1 and P2) are estimated using a linear fit for the three sections of the curve, and are marked with red dots. The coefficients of the functions were estimated as  $-5.14e07$ ,  $4.63e07$ ,  $42.89e07$ ,  $4.34e07$ ,  $-22.56e07$ ,  $5.15e07$ , while the critical moments  $M_{cr1}$  and  $M_{cr2}$  are  $5.63e-03$  Nm and  $1.34e-02$  Nm respectively. The results of the approximation are shown in Fig. 13.  $E_{eff}$  is then derived, as shown in Eq. (11), and serves as an input to the PRBM for calculating the stiffnesses and angular deformations of the torsional springs of the model

$$E_{eff} = \begin{cases} a_1 \cdot M + b_1; & \text{for } M \leq M_{cr1} \\ a_2 \cdot M + b_2; & \text{for } M_{cr1} > M > M_{cr2} \\ a_3 \cdot M + b_3; & \text{for } M \geq M_{cr2} \end{cases} \quad (11)$$



**Fig. 13.** Comparison between  $E_n$  and its multilinear approximation  $E_{eff}$ , which is used to define the torsional spring stiffnesses and angular deformations.

In Fig. 14, the position of the tip of the arc for an increasing prescribed rotation is presented. The model is deformed until  $4\pi$  radians. In the plots, the measurements of the tip position from FEA are marked with circles. The model with the lowest number of segments (2 segments) largely overpredicts the deformation, as shown in Fig. 14(a), whereas the models with three or more segments give a better approximation of the deformation. The MSE for the different number of segments is given in Table 3. Similar to the NiTi model, a higher number of segments ( $n$ ) results in a lower error between the PRBM and FEA. This is the most significant when comparing the PRBM with 2 and 12 segments, where the MSE is  $9.91e-04 \text{ m}^2$  and  $2.04 e-07 \text{ m}^2$  respectively.

In Fig. 14(b), the case with 12 segments is presented, which similar to the calculated error, shows a good prediction of the arc tip deformation. This means that the PRBM incorporating material nonlinearity can approximate both symmetric and asymmetric material curves for large deformations.

### 3.2.3. Experimental testing

To further study material nonlinearity, the folding CM was 3D-printed using TPU and the deflection was measured under applied load. The printing parameters that were used are presented in Appendix B. The CM was designed to have a hook feature for loading hanging masses, while the opposite side is fixed. Each specimen was marked with three dots to track the deflection as the load was increased (Fig. 15). These dots are labeled A, B, and C, such that A is a fixed point where the specimen is clamped, and the deflection of points B and C are measured.

To minimize the likelihood of error, and to verify the repeatability of the experiment, each specimen was tested individually through a complete loading cycle. The masses used in the experiment ranged from 0 to 200.3 grams, corresponding to forces of 0 to 1.962 N. The CM was fixed in a vise grip near point A, while the rest of the CM was free to deform. A digital photo was taken after each load was applied, and this resulted in 81 images for each specimen. The initial and final position of one specimen is highlighted in Figs. 16(a) and (b). There is some deformation that is evident before the CM is loaded that must be accounted for when the experimental data is compared with FEA later in this work. After the load is removed, there is a time-dependent recovery of strain in Fig. 16 (c) that is not considered but can be attributed to the viscoelastic property of hyperelastic materials.

After the three specimens were tested, the image processing software, Fiji (ImageJ) [35], was used to track the deflection throughout the experiment. The TrackMate plugin [36,37] was then used to capture the deflection path of points A, B, and C. A differences of gaussian (DoG) algorithm was selected to automatically detect the location of these three points after the image was converted to grayscale.

Fig. 17 shows the deflection path of points A, B, and C, which are at the centroids of the respective tracking circles, from its unloaded position to its final loaded position. Ideally, the path shown at point A should be single point, since the CM is clamped at that location. However, due to small shifts in the camera position while the pictures were being taken, the images were translated slightly relative to each other. To account for this error in the experimental results, the shift in  $x$  and  $y$  at point A were subtracted from the  $x$  and  $y$  coordinates of points B and C for each load.

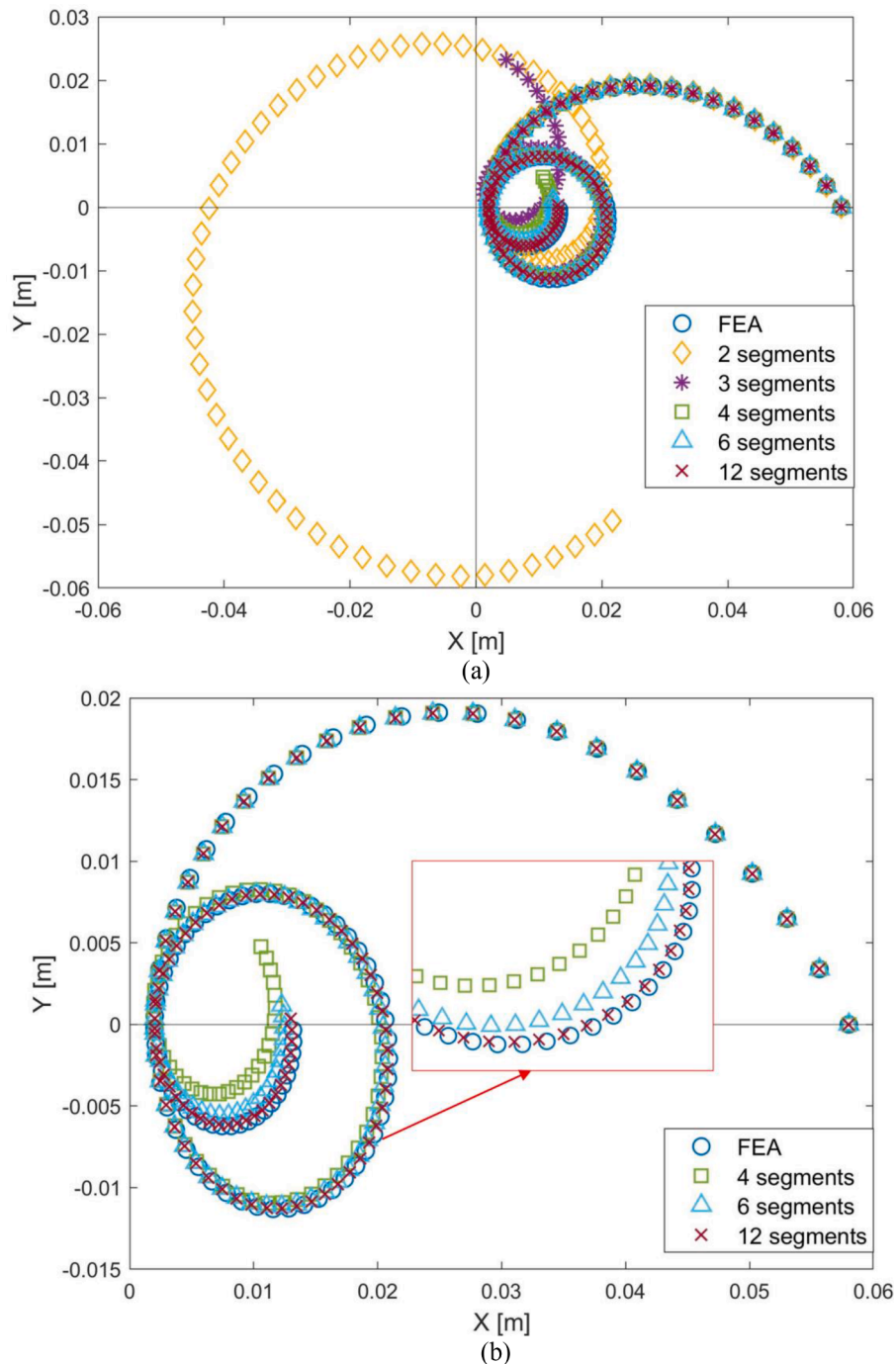


**Fig. 14.** Comparison of the segmented PRBM tip deflection for  $n = 2$  to  $12$  segments with FEA (a) and a zoomed in view of the PRBM tip deflection for a higher number of segments and a rotation of  $4\pi$  rad (b).

To validate the results of the experiment, the CM deflection at points A, B, and C was compared with a 2D model in COMSOL. The out-of-plane thickness of the model is 4 mm, which is the thickness of the arc of the 3D-printed model. The boundary and loading conditions are shown in Fig. 18. The applied load remains in the positive y-direction throughout the motion to represent the weight, or the force due to gravity acting on the hanging masses. The model is loaded from 0 to 1.96 N with 100 steps and with geometric nonlinearity enabled. Material nonlinearity is included by using the uniaxial data shown in Fig. 9 for TPU 95A. A fully-coupled, constant Newton solver with the Anderson acceleration stabilization method is used.

**Table 3**  
MSE between FEA and PRBM tip deflection for a hyperelastic material (TPU) and a different number of segments

Number of segments	MSE (m <sup>2</sup> )
2	9.91e-04
3	4.84e-05
4	3.22e-06
6	4.10 e-07
12	2.04 e-07

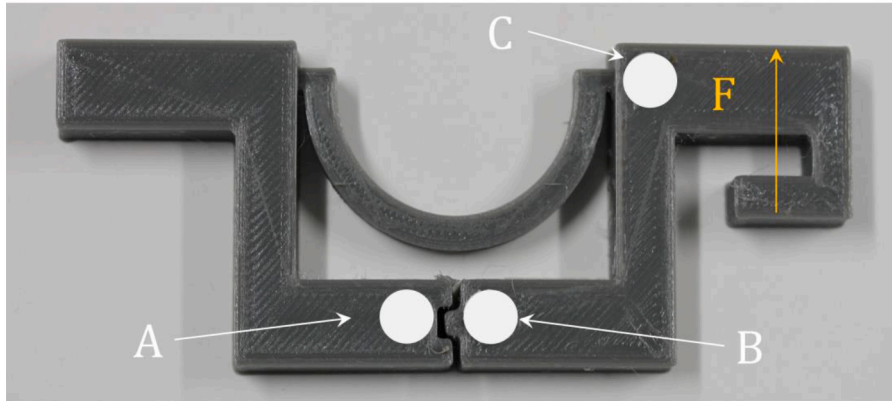


**Fig. 15.** 3D-printed CM with an applied load, F, and deflection points A, B, and C.

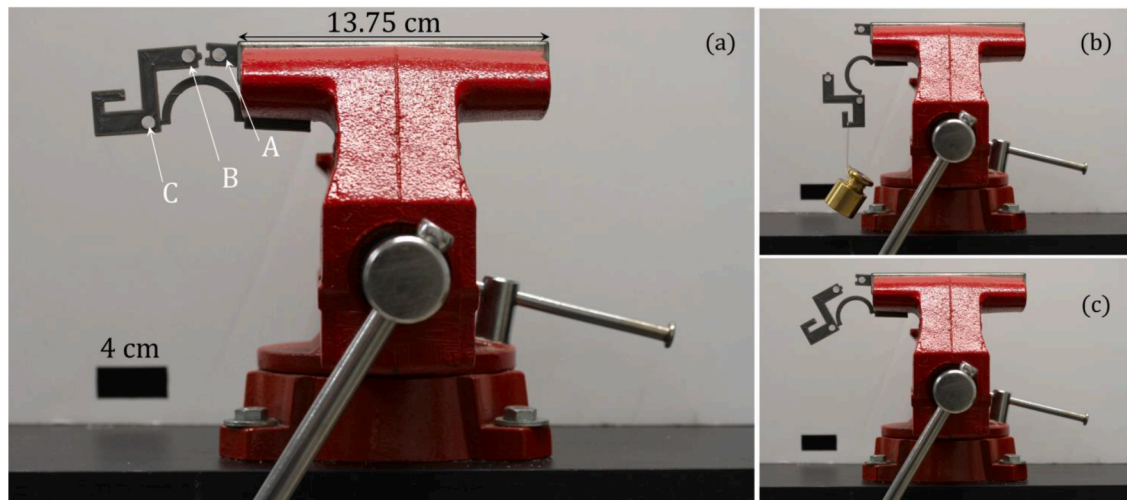


**Fig. 16.** Deflection of specimen at the initial position (a), the final position for a load of 1.962 N (b), and post-testing position representing strain recovery after load removal (c).

### 3.2.4. Results of experiment and discussion

The measured deflections of points A, B, and C on the three printed specimens were averaged and plotted against the FEA model. Fig. 19 shows the plot of the average ( $\pm$  one standard deviation) experimental results and the FEA results, where the data points from the FEA model were adjusted to account for the initial deformation of the folding CM in the experiment. It can be seen that there is good agreement between FEA and the experiment for the points along path C in that these points lie within the standard deviation band. The points along path B do show some deviation from the experimental average as the applied load is increased; however, the overall shape of the two curves is similar. The mean-squared error for paths B and C were calculated to evaluate the level of agreement. The FEA data was interpolated at the x-coordinates measured in the experiment. The MSE for paths B and C are  $8.63\text{e-}05\text{ m}^2$  and  $2.91\text{e-}06\text{ m}^2$  respectively.

While the results shown in Fig. 19 show good agreement between the experimental and FEA curves, there are some sources of error

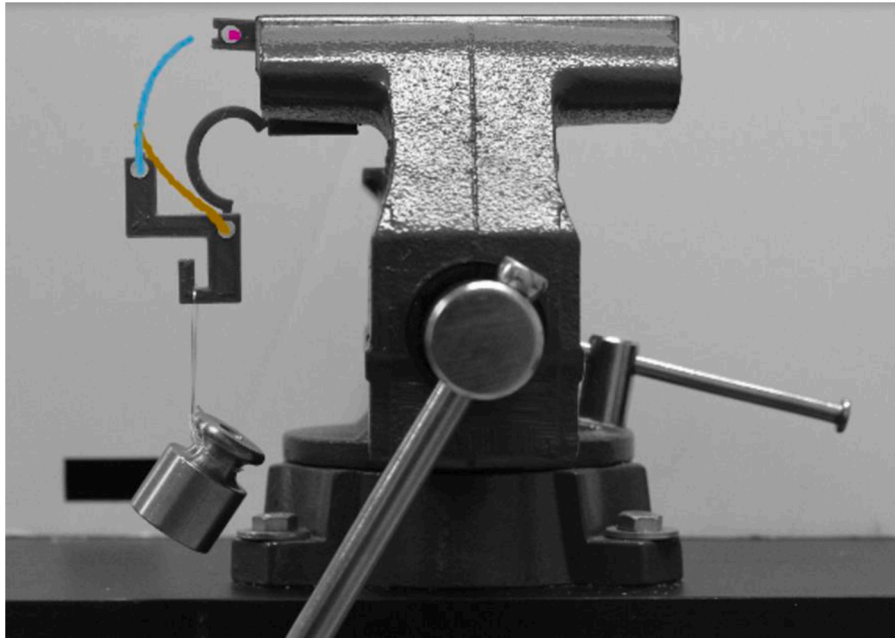


Fig. 17. Deflection path of points A, B, and C using TrackMate.

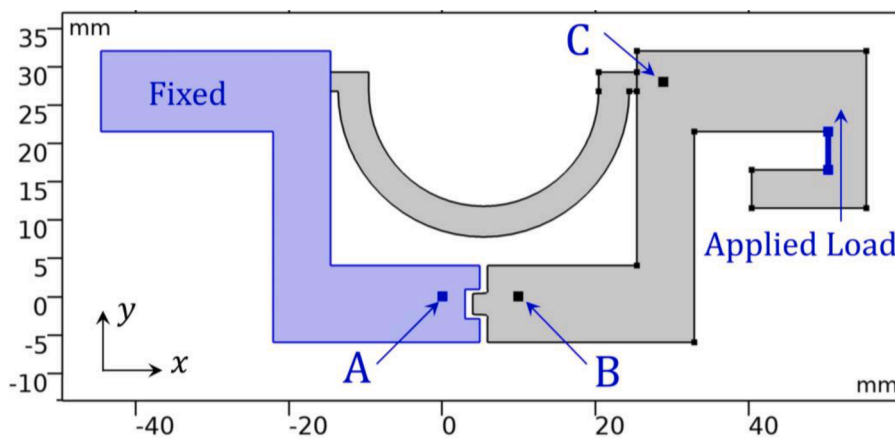


Fig. 18. CM model with a fixed boundary condition and load in the positive y-direction.

that can explain the differences between the two results. First, there could be human error during the experiment itself in that the camera shifted slightly between pictures. Even though this is accounted for in the final measurements, the images themselves could be distorted if the camera rotated slightly. Another factor could be that, since the CM is not completely rigid in the thicker section where it is clamped, the CM could experience some local deformations where it is not fully constrained in the vise grip. As mentioned in the previous section, the modeling of the CM in FEA does not account for any time-dependent behavior such as creep, stress-relaxation, and hysteresis. Fig. 16(c) demonstrates that there is some amount of permanent deformation in the CM after the final mass is removed. The error caused by the elastic recovery of the material, when the masses are loaded and unloaded, could be compounded throughout the experiment. Lastly, the 3D-printing process can introduce both geometric and material changes in the CM that affect its final performance. There could be differences in the internal structure of the parts due to the printing process, such as porosity and density, that may influence the mechanical behavior of the CM.

#### 4. Summary and conclusions

CMs have showed great potential in several applications such as energy absorption and shape morphing. To build on research in this area, a novel design of folding CM is modeled using nonlinear materials and considering large deformations. In this paper, a segmented PRBM for a folding CM is developed by segmenting the semicircular arc and developing a PRBM for each arc, which

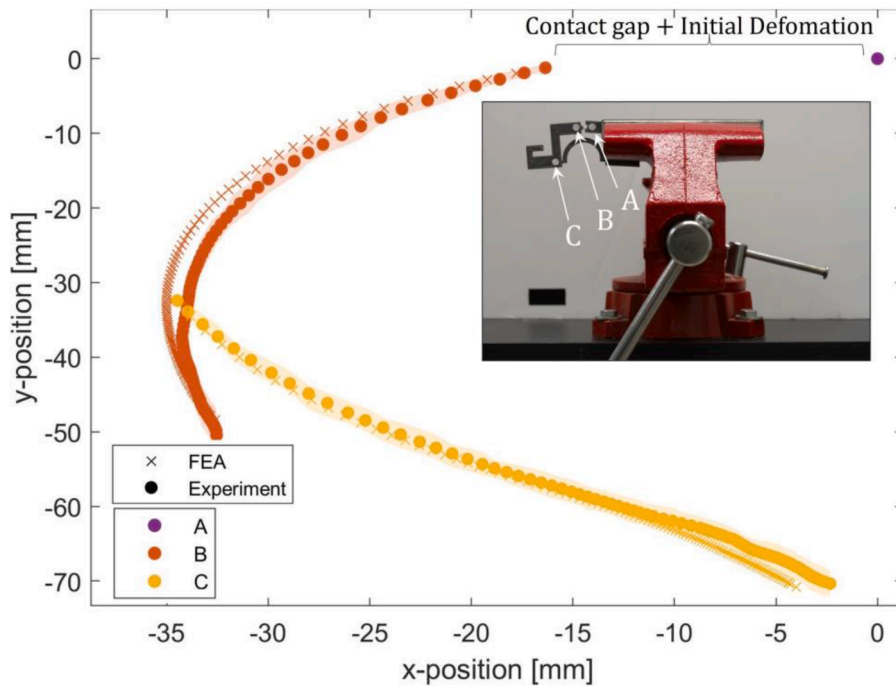


Fig. 19. Comparison of the deflection path of points A, B, and C for the experiment and FEA model, with +/- one standard deviation band.

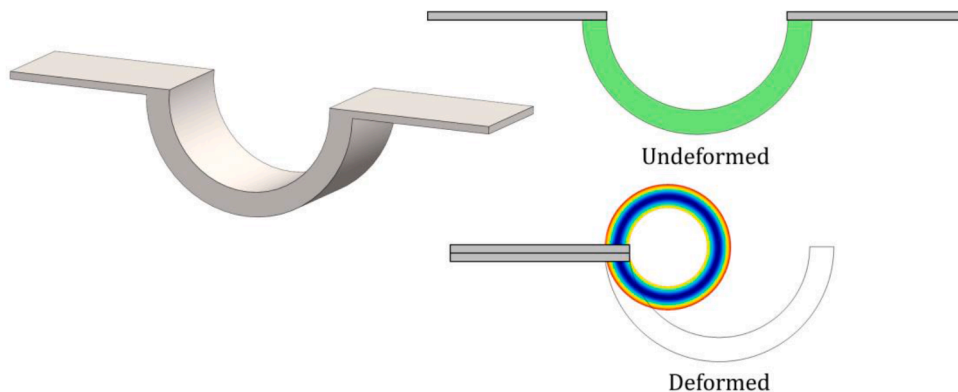


Fig. 20. Application of a CM as a compliant joint in an origami structure showing its undeformed position and deformed position for a full fold of  $\pi$  rad.

increases the overall accuracy of the model. The PRBM is compared to FEA for a different number of segments, from 1 to 12 segments. The results show that the error for the PRBM decreases when more segments are introduced. The addition of nonlinearity in the model augments the error between the PRBM and FEA for a smaller number of segments, since both material and geometric nonlinearity is involved. Thus, to accurately model a CM that deforms beyond the maximum expected physical deformation of  $\pi$  radians, or for large deformations, a higher number of segments may be chosen to provide a better approximation of the tip position. However, the results presented for the number of segments studied are dependent on the geometry, material properties, and the loading conditions.

The segmented PRBM is then modified to account for material nonlinearity. Since the effective elastic modulus depends on the stress, the spatial distribution of this property is not uniform. By approximating the effective modulus with a multilinear function, the nonlinearity can be adequately captured. Two case studies are presented, one with superelastic NiTi and one with hyperelastic TPU. For both models, an increase in the number of segments decreased the error between the PRBM and the FEA results for the deflection of the mechanism. Additionally, this means that the proposed method for modeling of nonlinear materials with PRB models can work for both symmetric and asymmetric material models.

Experimental testing of a 3D-printed CM of TPU shows that the deflection of the folding CM under an applied load is in good agreement FEA. Future work aims to look at how the current PRBM could be extended to include a tip force, such that the analytical approach could also be used to validate the experimental results. The PRBM, using the equations defined in this work, is limited to

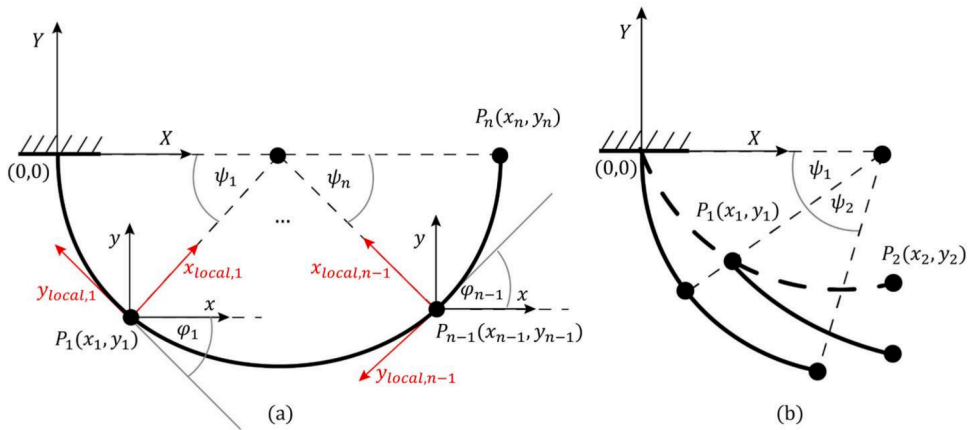


Fig. A.1. Rotation of axes of the local coordinate system to the global coordinate system (a) and translation and deformation of the connected segments (b).

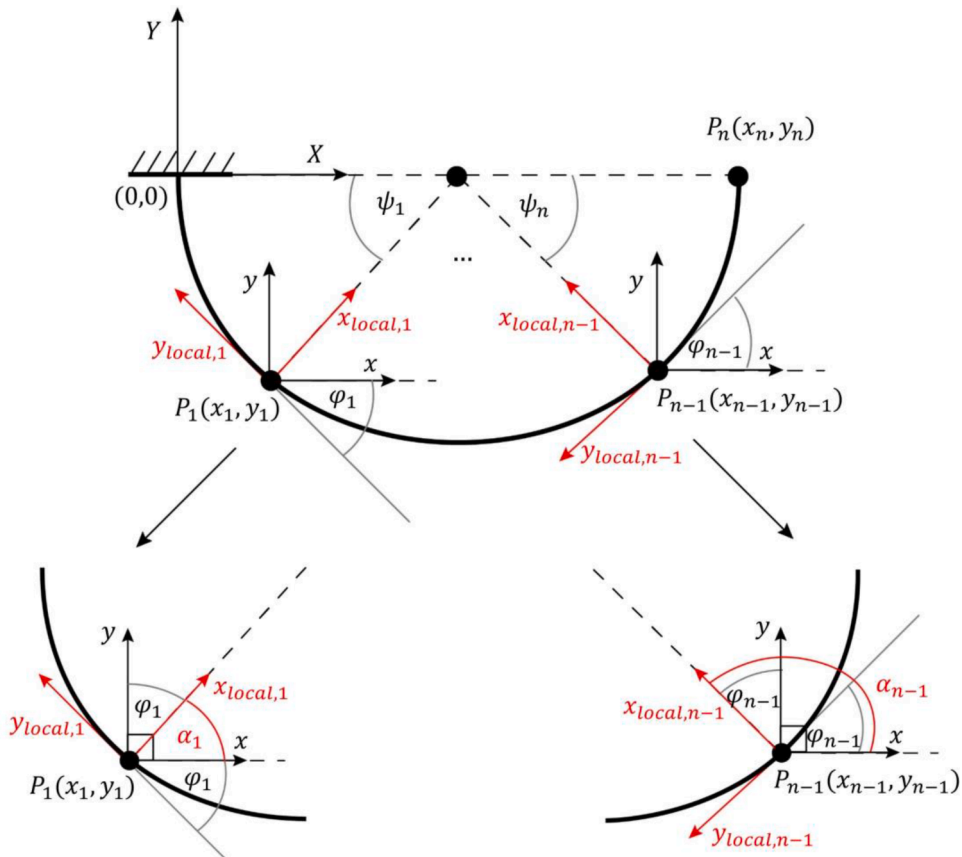


Fig. A.2. Definition of rotation angle between the local and global coordinate systems that define the orientation of each segment and the final tip locations.

solely tip moments. However, redefining the current PRBM to be suitable for both a moment and a force, which has been studied in literature for initially curved beams and linear-elastic material [38], would make our approach even more robust as we would additionally consider both material and geometric nonlinearity.

Compliant mechanisms with complex geometry and nonlinear materials require a high amount of computational time if the designs rely only on FEA analysis with parametric analysis or optimization. Introducing the segmented PRBM into a formal design optimization routine and considering self-contact of the “folding C3M” are the next steps in this research. To capture the effect of the contact

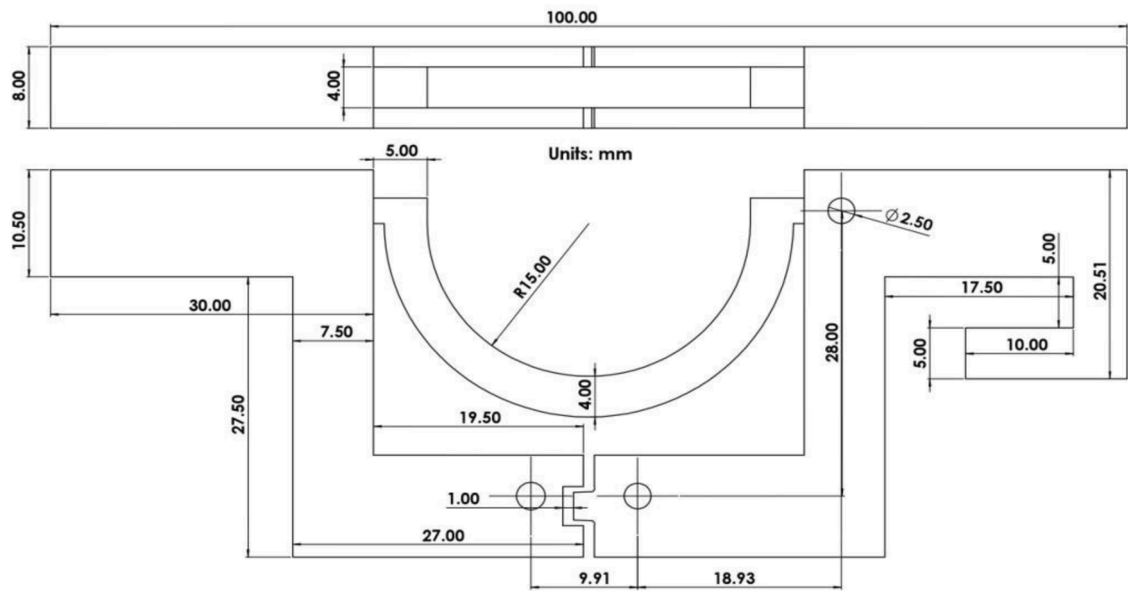
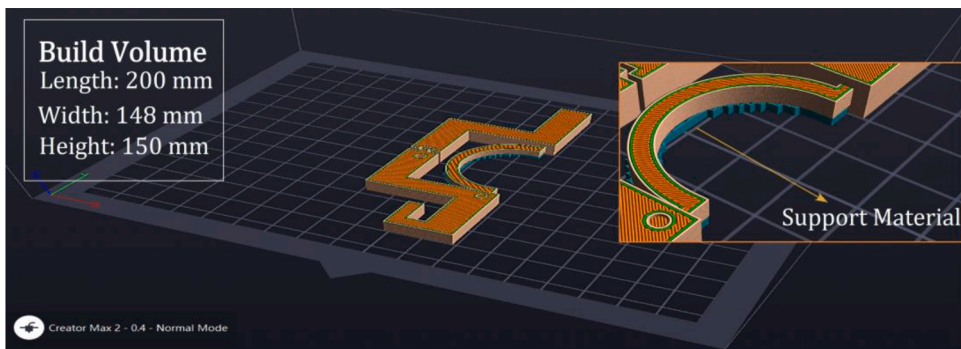


Fig. B.1. Dimensions of CM model in CAD.



(a)



(b)

Fig. B.2. Build plate orientation and location of support material (a) and the three 3D-printed CM specimens (b).

Table B.1  
3D-printing process parameters used for CM

Print Speed	Extruder Temp.	Bed Temp.	Infill Density	Layer Height	Retraction Speed	Retraction Distance
30 mm/s	210°C	60°C	100%	0.1 mm	15 mm/s	1.5 mm

**Table B.2**  
Dimensional and material properties of printed specimens

	Specimen 1	Specimen 2	Specimen 3
Mass	14.80 g	15.10 g	15.00 g
In plane-thickness	3.95 mm	3.97 mm	3.99 mm
Out of plane-thickness	4.21 mm	4.10 mm	4.23 mm

member, an additional nonlinear translational spring could be added to the PRBM. Future research will also be focused on design optimization of the CM for other applications such as energy absorption, shape morphing, origami engineering, and soft grasping. Fig. 20 illustrates a potential application of the folding CM for a full folding compliant joint in an origami structure is shown. Since the CM analyzed in this paper can attain high deformations, it would be useful for allowing an origami structure to achieve a complete fold from 3D to a 2D structure and vice versa. Additionally, the shape memory effect of the nonlinear NiTi material implemented in these joints could introduce thermal actuation to allow for self-folding origami.

### Declaration of Competing Interest

The authors declare that they have no known competing financial interests or personal relationships that could have appeared to influence the work reported in this paper.

### Acknowledgements

We would like to thank the organizers of ReMAR 2021 for inviting us to submit a journal-quality version of our paper. This work serves as an extended version of the ReMAR 2021 conference paper, in which a segmented PRBM capable of capturing large deflections due to geometric nonlinearity as well as material nonlinearity through superelastic NiTi was developed. The extension of this paper in the current work demonstrates the robustness of the segmented PRBM approach for other nonlinear materials, such as hyperelastic TPU, and the potential for experimental validation of the folding CM through 3D-printing.

### Appendix A. Coordinate transformation of PRBM tip deflection

The coordinates of the tip point of the arc are the coordinates of the end point of the  $n$ th segment in the global coordinate system ( $X$ ,  $Y$ ) as shown in Fig. A.1(a). The deformation of each segment is calculated in its local coordinate system ( $x_{local,i}$ ,  $y_{local,i}$ ). Then each segment is rotated with respect to the previous one in the global coordinate system. The local coordinate system of the first segment is the same as the global one, and the local coordinate systems of the other segments are rotated with respect to this coordinate system as shown in Fig. A.1(a). Additional to the rotation, the local tip deformation of each segment is also translated to the end point of the previous segment after the deformation in the global coordinate system, as shown in Fig. A.1(b).

The rotation of the  $i^{th}$  segment to the global coordinate system can be calculated using Eq. (A.1), where it is rotated in the clockwise direction by the angle  $\alpha_{i-1}$ .

$$\alpha_{i-1} = -\frac{\pi}{2} - \varphi_{i-1} \quad i = 1, 2, \dots, n \quad (A.1)$$

The angle  $\varphi_{i-1}$  is defined as the tangent angle of the segment curvature at the point  $P_{i-1}$ .

$$\varphi_{i-1} = \tan^{-1} \left( \frac{df}{dx} \Big|_{x_{i-1}} \right) \quad i = 1, 2, \dots, n \quad (A.2)$$

The curvature function  $f(x)$  is defined as a semicircle with radius,  $R$ , and center at the point  $(R, 0)$ .

$$f(x) = -\sqrt{R^2 - (x - R)^2} \quad (A.3)$$

The orientation of the segments dictates the contribution to the final tip displacement as shown in Fig. A.2.

The coordinates of the end point are a sum of the positions of all the other end points in the global coordinate system.

$$x_{tip} = \sum_{i=1}^n x_{global,i} \quad i = 1, 2, \dots, n \quad (A.4)$$

$$y_{tip} = \sum_{i=1}^n y_{global,i} \quad i = 1, 2, \dots, n \quad (A.5)$$

which means that the tip final equations are:

$$x_{iip} = x_{local,1} + \sum_{i=2}^n x_{local,i} \cdot \cos(\alpha_{i-1} + (i-1) \cdot (-\theta_{1i} - \theta_{2i})) + y_{local,i} \cdot \sin(\alpha_{i-1} + (i-1) \cdot (-\theta_{1i} - \theta_{2i})) \quad (A.6)$$

$$y_{iip} = y_{local,1} + \sum_{i=2}^n -x_{local,i} \cdot \sin(\alpha_{i-1} + (i-1) \cdot (-\theta_{1i} - \theta_{2i})) + y_{local,i} \cdot \cos(\alpha_{i-1} + (i-1) \cdot (-\theta_{1i} - \theta_{2i})) \quad (A.7)$$

Since the  $(x_i, y_i)$  values are dimensionless, they need be scaled by the length of the arc,  $L$ , which is the circumference of the half-circle defined by its radius  $R$ , where  $(L = R\pi)$ . The difference in the results for the baseline PRBM with one segment and the segmented model are described further in this paper.

## Appendix B. 3D-Printing of CM specimens using TPU

To further study material nonlinearity, the CM model presented in Fig. B.1 was 3D-printed and tested under an applied load. Support material was added under the semicircular arc as shown in Fig. B.2(a). Three specimens as shown in Fig. B.2(b) were printed with TECBEARS TPU 95A filament on a FlashForge Creator Max 2 printer. Due to the viscous nature of TPU, parts printed using this material commonly have issues with stringing or oozing of filament that can affect the quality, dimensional accuracy, and mechanical behavior of the final part. To reduce this problem, the specimens were printed one at a time with the process parameters shown in Table B.1. The CM was modeled in SolidWorks and sliced using the FlashPrint software provided by FlashForge.

Although the specimens were printed on the same printer, there were some differences in their final dimensions and mass as shown in Table B.2. This could be due to external factors such as temperature, humidity, or slight variations in the printing process itself. The as-designed in-plane and out-of-plane thicknesses are both 4 mm, and the specimens are very close to this value. However, it should be noted that the deviation of these measurements from the as-designed CAD part may play a role in the final mechanical behavior of each CM specimen.

## References

- [1] N.D. Mankame, G.K. Ananthasuresh, Synthesis of contact-aided compliant mechanisms for non-smooth path generation, *Int. J. Numer. Methods Eng.* 69 (12) (2007) 2564–2605.
- [2] N.D. Mankame, G.K. Ananthasuresh, Topology optimization for synthesis of contact-aided compliant mechanisms using regularized contact modeling, *Comput. Struct.* 82 (15–16) (2004) 1267–1290.
- [3] J.P. Calogero, M.I. Frecker, Z. Hasnain, J.E. Hubbard, Dual optimization of contact-aided compliant mechanisms for passive dynamic shape change, *AIAA J* 56 (9) (2018) 3745–3756.
- [4] B.V.S.N. Reddy, S.V. Naik, A. Saxena, Systematic synthesis of large displacement contact-aided monolithic compliant mechanisms, *J. Mech. Des. Trans. ASME* 134 (1) (2012) 1–12.
- [5] Y. Tummala, A. Wissa, M. Frecker, J.E. Hubbard, Design and optimization of a contact-aided compliant mechanism for passive bending, *J. Mech. Robot.* 6 (3) (2014) 1–9.
- [6] V. Mehta, M. Frecker, G.A. Lesieutre, Two-step design of multicontact-aided cellular compliant mechanisms for stress relief, *J. Mech. Des. Trans. ASME* 134 (12) (2012) 1–12.
- [7] V. Mehta, M. Frecker, G.A. Lesieutre, Stress relief in contact-aided compliant cellular mechanisms, *J. Mech. Des. Trans. ASME* 131 (9) (2009) 0910091–09100911.
- [8] S.A. Cirone, G.R. Hayes, B.L. Babcox, M. Frecker, J.H. Adair, G.A. Lesieutre, Design of contact-aided compliant cellular mechanisms with curved walls,” *Artic. J. Intell. Mater. Syst. Struct.* 23 (16) (2012) 1773–1785.
- [9] J.E. Hyland, M.I. Frecker, G.A. Lesieutre, Optimization of honeycomb contact aided compliant cellular mechanism for strain energy absorption, *Proceedings of the ASME Design Engineering Technical Conf 4 (Parts A and B)* (2012) 311–320.
- [10] J. Jovanova, A. Nastevska, M. Frecker, Tailoring energy absorption with functional grading of a contact-aided compliant mechanism, *Smart Mater. Struct.* 28 (8) (2019).
- [11] J. Jovanova, A. Nastevska, M. Frecker, Functionally graded cellular contact-aided compliant mechanism for energy absorption, in: *ASME 2018 Conference on Smart Materials, Adaptive Structures and Intelligent Systems 2, SMASIS*, 2018, p. 2018.
- [12] Y. Tummala, M.I. Frecker, A. Wissa, J.E. Hubbard, Design and optimization of a bend-and-sweep compliant mechanism, *Smart Mater. Struct.* 22 (9) (2013).
- [13] P. Bilancia, G. Berselli, S. Magleby, L. Howell, On the modeling of a contact-aided cross-axis flexural pivot, *Mech. Mach. Theory* 143 (2020).
- [14] Y. Moon, Bio-mimetic design of finger mechanism with contact aided compliant mechanism, *Mech. Mach. Theory* 42 (5) (2007) 600–611.
- [15] K.W. Eastwood, P. Francis, H. Azimian, A. Swarup, T. Looi, J.M. Drake, H.E. Naguib, Design of a Contact-Aided Compliant Notched-Tube Joint for Surgical Manipulation in Confined Workspaces, *ASME. J. Mechanisms Robotics.* 10 (1) (2017).
- [16] P. Kumar, R.A. Sauer, A. Saxena, On topology optimization of large deformation contact-aided shape morphing compliant mechanisms, *Mech. Mach. Theory* 156 (2021), 104135.
- [17] L. Liu, J. Xing, Q. Yang, Y. Luo, Design of Large-Displacement Compliant Mechanisms by Topology Optimization Incorporating Modified Additive Hyperelasticity Technique, *Math. Probl. Eng.* (2017).
- [18] X.S. Zhang, H. Chi, Z. Zhao, Topology optimization of hyperelastic structures with anisotropic fiber reinforcement under large deformations, *Comput. Methods Appl. Mech. Eng.* 378 (2021), 113496.
- [19] J. Joo, S. Kota, Topological Synthesis of Compliant Mechanisms Using Nonlinear Beam Elements, *Mechanics Based Design of Structures & Machines* 32 (1) (2004) 17–38.
- [20] Z. Li, X. Zhang, Topology optimization of compliant mechanisms with geometrically nonlinear, in: *International Technology and Innovation Conference (ITIC)*, 2006, pp. 477–482.
- [21] B.S. Lazarov, M. Schevenels, O. Sigmund, Robust design of large-displacement compliant mechanisms, *Mechanical Sciences* (2011).
- [22] C. Chu, G. Graf, D.W. Rosen, Design for Additive Manufacturing of Cellular Structures, *Comput. Aided. Des. Appl.* 5 (5) (2008) 686–696.
- [23] A.N. Danun, P.D. Palma, C. Klahn, M. Meboldt, Building Block Synthesis of Self Supported Three-Dimensional Compliant Elements for Metallic Additive Manufacturing, *J. Mech. Des. Trans. ASME* 143 (5) (2021).
- [24] L.L. Howell, *Compliant Mechanisms*, Wiley, 2001.

- [25] M. Jin, B. Zhu, J. Mo, Z. Yang, X. Zhang, L.L. Howell, A CPRBM-based method for large-deflection analysis of contact-aided compliant mechanisms considering beam-to-beam contacts, *Mech. Mach. Theory* 145 (2020), 103700.
- [26] C.A. Mattson, L.L. Howell, S.P. Magleby, Development of Commercially Viable Compliant Mechanisms Using the Pseudo-Rigid-Body Model: Case Studies of Parallel Mechanisms, *J. Intell. Mater. Syst. Struct.* 15 (3) (2004), 195–22, 24.
- [27] Y.Q. Yu, S.K. Zhu, 5R pseudo-rigid-body model for inflection beams in compliant mechanisms, *Mech. Mach. Theory* 116 (2017) 501–512.
- [28] G. Berselli, F. Parvari Rad, R. Vertechy, V. Parenti Castelli, Comparative evaluation of straight and curved beam flexures for selectively compliant mechanisms, in: *IEEE/ASME International Conference on Advanced Intelligent Mechatronics (AIM): Mechatronics for Human Wellbeing*, 2013, pp. 1761–1766.
- [29] A. Nastevska, M. Frecker, Design of Compliant Joints for Large Scale Structures, in: *ASME Conference on Smart Structures Adaptive Structures and Intelligent Systems*, 2020, pp. 1–10.
- [30] V.K. Venkiteswaran, H.J. Su, Pseudo-rigid-body models for circular beams under combined tip loads, *Mech. Mach. Theory* 106 (2016) 80–93.
- [31] F. Auricchio, R.L. Taylor, J. Lubliner, Shape-memory alloys: Macromodelling and numerical simulations of the superelastic behavior *Universita' di Roma &quot; Tor Vergata&quot;*, *Comput. Methods Appl. Mech. Engrg.*, vol. 146 (1997) 281–312.
- [32] S.W. Robertson, A.R. Pelton, R.O. Ritchie, Mechanical fatigue and fracture of Nitinol, *Int. Mater. Rev.* 57 (1) (2012) 1–37.
- [33] P. Platek, K. Rajkowski, K. Cieplak, M. Sarzyński, J. Małachowski, R. Woźniak, J. Janiszewski, Deformation Process of 3D Printed Structures Made from Flexible Material with Different Values of Relative Density, *Polymers* 12 (2020) 2120.
- [34] A. Rohatgi, “WebPlotDigitizer,” **Version 4.5**, 2021.
- [35] J. Schindelin, I. Arganda-Carreras, E. Frise, V. Kaynig, M. Longair, T. Pietzsch, S. Preibisch, C. Rueden, S. Saalfeld, B. Schmid, JY. Tinevez, DJ. White, V. Hartenstein, K. Eliceiri, P. Tomancak, A. Cardona, Fiji: an open-source platform for biological-image analysis, *Nat. Methods* 9 (7) (2012) 676–682.
- [36] D. Ershov, MS. Phan, J.W. Pylvänäinen, S.U. Rigaud, L.L.B. Arthur Charles-Orszag, J.R.W. Conway, R.F.Laine, N.H.Roy, D. Bonazzi, G. Duménil, G. Jacquemet, JY. Tinevez, “Bringing TrackMate in the era of machine-learning and deep-learning,” *bioRxiv*, 2021.
- [37] JY. Tinevez, N. Perry, J. Schindelin, GM. Hoopes, GD. Reynolds, E. Laplantine, SY. Bednarek, SL. Shorte, KW. Eliceiri, TrackMate: An open and extensible platform for single-particle tracking, *Methods* 115 (2017) 80–90.
- [38] V.K. Venkiteswaran, H.J. Su, Pseudo-Rigid-Body Models of Initially-Curved and Straight Beams for Designing Compliant Mechanisms, in: *Proceedings of the ASME 2017 International Design Engineering Technical Conferences and Computers and Information in Engineering Conference*, Volume 5A: 41st Mechanisms and Robotics Conference, 2017.